

## Estimation of cirrus cloud effective ice crystal shapes using visible reflectances from dual-satellite measurements

Helene Chepfer

Laboratoire de Meteorologie Dynamique, Ecole Polytechnique, Palaiseau, France

Patrick Minnis, David Young, and Louis Nguyen

NASA/Langley Research Center, Hampton, Virginia, USA

Robert F. Arduini<sup>1</sup>

Science Applications International Corporation, Hampton, Virginia, USA

Received 8 December 2000; revised 20 November 2001; accepted 30 November 2001; published 14 December 2002.

[1] This study develops and examines a multiangle, multisatellite method for determining effective cloud particle shapes from reflectances observed at visible wavelengths. The technique exploits the significant differences in the various cloud particle shape phase functions near the backscatter direction to infer particle shape from a combination of views from a near-backscatter angle and a side scattering angle. Adding-doubling calculations confirm that the optimal viewing combinations include one near-backscatter angle and another between 60° and 150°. Sensitivity to shape increases with solar zenith angle. A total of 28 collocated, visible images from pairs of currently operating meteorological satellites with the desired viewing combinations were analyzed for particle shape. Matching reflectances from images with optimal viewing angles clearly separates water droplet from ice crystal clouds. Reflectance pairs from matched pixels containing ice crystals can be explained by the range of selected microphysical models. The most common retrieved shapes correspond to combinations of hexagonal compacts (aspect ratio of unity), hexagonal columns, and bullet rosettes. Although no single microphysical model can account for the observed variability, taken together, the models used for retrieving cloud particle size by the Clouds and the Earth's Radiant Energy System and the Moderate Resolution Imaging Spectroradiometer Projects can account for most of the reflectance variability observed in this limited data set. Additional studies are needed to assess the uncertainties in retrieved shapes due to temporal and spatial mismatches, anisotropic and bright background reflectances, and calibration errors and to validate the retrieved shapes. While applicable to a limited number of dual-satellite viewing combinations for current research and operational meteorological satellites, this approach could be used most extensively to derive effective particle size, shape, and optical depth from a combination of an imaging satellite in an L1 orbit, like Triana, and any other lower Earth orbiting satellites. *INDEX TERMS:* 0320 Atmospheric Composition and Structure: Cloud physics and chemistry; 1640 Global Change: Remote sensing; 1610 Global Change: Atmosphere (0315, 0325); 0394 Atmospheric Composition and Structure: Instruments and techniques; *KEYWORDS:* ice clouds, crystal shape, geostationary satellites

**Citation:** Chepfer, H., P. Minnis, D. Young, L. Nguyen, and R. F. Arduini, Estimation of cirrus cloud effective ice crystal shapes using visible reflectances from dual-satellite measurements, *J. Geophys. Res.*, 107(D23), 4730, doi:10.1029/2000JD000240, 2002.

### 1. Introduction

[2] Cirrus clouds play a major role in the Earth radiation energy balance and hydrological cycle. On average, they cover more than 20% [Liao *et al.*, 1995] of the Earth and

interact with the radiation through two opposing effects [Liou, 1986]. They reflect incident solar radiation, and so tend to cool the Earth-atmosphere system. Conversely, they intercept some or all of the infrared radiation emitted by the ground and the lower layers of the atmosphere causing warming of the system. To accurately account for these radiative effects of cirrus clouds in climate models while maintaining the correct amount of frozen water, it is necessary to understand both the macrophysical (e.g., areal coverage, altitude, ice water path, temperature, and vertical

<sup>1</sup>Now at NASA/Langley Research Center, Hampton, Virginia, USA.

extent) and microphysical (e.g., particle size and shape distributions and orientation) properties of cirrus clouds. The size and shape distributions govern the underlying optical properties (extinction efficiency, scattering phase function, and single scattering albedo) that, when combined with the macrophysical properties, determine the optical depth and, hence, the amount of absorption, emission, and reflection. To simplify discussion and radiative transfer model execution, distributions of cloud particle size and shape are usually replaced by effective size (radius or diameter) and effective shape, respectively. Although significant advances have been made both in establishing the spatial and temporal distribution of cirrus cloud properties and in modeling the processes that produce cirrus clouds, the accuracies of current cirrus property climatologies and the capability for simulating cirrus processes remain insufficient for adequately accounting for cirrus clouds in climate models. One major source of uncertainty is the limited knowledge of the spatial (vertical and horizontal) and temporal distributions of effective ice crystal shape. Remote sensing from satellites is the only feasible way to derive a global climatology of cloud properties, and ice crystal habit is no exception. In this study, a new approach is developed for discerning effective cirrus ice crystal shape from dual-satellite measurements that, when applied to current and, especially, possible future satellite systems, may provide relatively high temporal and spatial distributions of this important parameter. Additionally, it can be used to assess the errors in current techniques that derive ice cloud optical depth with the assumption of a constant particle shape.

[3] During the last 2 decades, data from several intensive field experiments [e.g., *Randall et al.*, 1996; *Raschke et al.*, 1998; *McFarquhar and Heymsfield*, 1996; *Toon and Mialke-Lye*, 1998] have shown the complexity and variability of cirrus cloud microphysical properties. In situ observations [e.g., *Heymsfield*, 1975; *Heymsfield and Platt*, 1984; *Heymsfield*, 1993; *Krupp*, 1991; *Francis et al.*, 1994] have revealed the range of ice crystal habits occurring in several midlatitude and a few equatorial cirrus clouds. These studies spurred the development of more realistic models of ice crystal optical properties [*Takano and Liou*, 1989; *Macke et al.*, 1996a, 1996b; *Yang and Liou*, 1998] based on local precise observations. Several techniques using spaceborne observations have been developed to study the global variability of microphysical properties at a global scale. The split-window method using two infrared channels [e.g., *Inoue*, 1985; *Giraud et al.*, 1997] has been used to determine effective ice crystal size for some cirrus clouds. A visible infrared solar-infrared split window technique (VISST) has been used to derive cloud phase and effective ice crystal size assuming hexagonal column shaped crystal distributions from Sun-synchronous [e.g., *Minnis et al.*, 1997] and midinclined [*Minnis et al.*, 1999] orbiting satellites. *Minnis et al.* [1993] used optical depths derived from two satellites simultaneously viewing the same clouds to distinguish water droplets from hexagonal ice columns. With the advent of more sophisticated sensors that measure reflectances and polarization at two or more angles from a single satellite, it became possible to determine effective particle shape [*Baran et al.*, 1999; *Chepfer et al.*, 2000] and degree of orientation [*Chepfer et al.*, 1999]. However, these new techniques are restricted in time and space coverage because the information content

in the multiangle views is limited by similarities in the ice crystal phase functions over a large range of scattering angle. The greatest reflectance differences among the various ice crystal shapes occur in the backscattering direction (i.e., near  $180^\circ$ ). Thus, the combination of measurements from near backscattering with those from an angle away from backscattering should provide the best sensitivity for distinguishing the effective shape of ice crystals.

[4] A new imager, the Earth Polychromatic Imaging Camera (EPIC), has been built and integrated into the Triana satellite that was designed for placement in a Lissajous orbit at the L1 point [*Valero et al.*, 1999]. The EPIC is a 10-channel CCD instrument that will measure ultraviolet, visible, and near-infrared radiances each hour with a nominal subsatellite resolution of 8 km. All of the channels match one or more of those currently operating on imagers carried by low-Earth orbit (LEO) and geostationary Earth orbit (GEO) satellites. The planned elliptical orbit around the Earth-Sun line (ESL) will vary slowly from  $3^\circ$  to  $15^\circ$  off of the ESL. At this location, the EPIC will view nearly all sunlit locations on the Earth at scattering angles between  $165^\circ$  and  $177^\circ$  depending on the time of the orbit.

[5] The goal of the current paper is to demonstrate the potential for exploiting such viewing conditions by coupling the nearly continuous Triana EPIC data or similar near-backscatter data from a subset of LEO or GEO measurements with reflected radiances measured nearly simultaneously from any other GEO or LEO satellite to retrieve cirrus cloud effective ice crystal shape. The crystal shape estimation method matches reflectance of the same cloud parcel measured at a common visible wavelength ( $\sim 0.65 \mu\text{m}$ ) from two different viewing directions. With the Triana and several other satellites, it should be possible to obtain unprecedented temporal resolution and spatial coverage of effective particle shape and size. More limited time and space coverage can be obtained with various pairs of LEO and GEO satellites. Section 2 is devoted to a theoretical sensitivity study highlighting the limitations and the potential of the proposed retrieval technique. Section 3 demonstrates the estimation technique applied to currently operating satellites using combinations of angles that would be viewed by Triana and another satellite. Sections 4 and 5 are devoted to discussion and conclusion, respectively.

## 2. Sensitivity Study

[6] To study the sensitivity of the bidirectional reflectances observed by a pair of satellites to ice crystal shape, the reflectances at two scattering angles  $\Theta$  were computed for different kinds of cirrus clouds: the first direction corresponds to observations from a satellite like Triana ( $\Theta = 168^\circ$ ,  $175^\circ$ ) and the second one to another satellite. To facilitate the discussion, the satellite in the near-backscatter position is, hereafter, referred to as Triana. The computations of solar light reflected by the atmosphere containing a cirrus cloud must include the optical properties of ice crystals composing the cirrus clouds (section 2.1) and multiple scattering effects using a radiative transfer code (section 2.2).

### 2.1. Ice Crystal Optical Properties

[7] It is assumed here that all of the cloud particles, except water droplets, are crystals composed of ice water

**Table 1.** Cloud Particle Models Considered in the Current Study<sup>a</sup>

Name	Crystal Shape	Crystal Size (Effective Diameter, m)	Asymmetry Factor	Computation Method
Ceres_contrail	compacts + columns	18	0.77	GO
Ceres_nov1	compacts + columns	75	0.82	GO
Ceres_big_crystal	compacts + columns	135	0.85	MT + GO
Modis_1	bullet-rosettes + plates + hollow column	9	0.75	GO + FDTD
Modis_2	bullet-rosettes + plates + hollow column	33	0.80	GO + FDTD
Modis_3	bullet-rosettes + plates + hollow column + aggregates	79	0.84	GO + FDTD
Modis_rough	bullet-rosettes + plates + hollow column	30	0.81	GO + FDTD
Iscpp	polycrystals	60	0.94	GO
Plates	plates (Q = 0.05)	40	0.85	GO
Columns	columns (Q = 2.5)	40	0.80	GO
Compacts	compacts (Q = 1)	40	0.70	GO
Bullet-rosette	bullet-rosettes	87	0.83	GO
Spheres_6	spheres	12	0.94	MT
Spheres_8	spheres	16	0.94	MT

<sup>a</sup>MT, Mie Theory; GO, Geometric Optic; GOM, Geometric Optic Modified; FDTD, Finite Differential Time Domain; Q, shape ratio.

that are randomly oriented in space. The retrieval of cirrus cloud microphysical properties from space-borne observations requires an a priori choice of several microphysical models that effectively cover the variety of different microphysical properties observed so far. In situ observations have mainly documented midlatitude cirrus clouds and rarely other types of cirrus clouds like those found in the tropics. The optical properties of other types of crystals not yet or rarely observed will not be represented in the selected range of crystal types.

[8] During the last 2 decades, several computational techniques have been developed to derive ice crystal optical properties. Each of them is adapted to shapes and/or sizes of ice crystals as follows (see *Mishchenko et al.* [1996] for a review).

1. Mie theory is used to compute spherical ice crystal or water droplet properties for various size distributions in different wavelength domains.

2. The simple Geometric Optics (GO) technique [e.g., *Wendling et al.*, 1979; *Takano and Liou*, 1989] enhanced with Fraunhofer diffraction is sufficient for single non-spherical ice crystals having simple shapes, like hexagonal columns and plates, and a large size compared to the wavelength (typically adapted to visible wavelengths for large cirrus cloud ice crystals).

3. Improved application of the GO method can be used to compute properties for more complex crystal shapes like bullet rosettes, hollow columns, aggregates [*Takano and Liou*, 1995], polycrystals [*Macke et al.*, 1996a], and nonperfect crystals having rough surfaces [*Macke et al.*, 1996b; *Yang et al.*, 2000].

4. A recent advancement has adapted the computation to particles having a size comparable to the wavelength by taking into account interference between the rays in using the FDTD (Finite Differential Time Domain) method [*Yang and Liou*, 1996, 1998].

5. The most recent improvements have led to the computation of optical properties for different particle size distributions of nonspherical particles [*Yang et al.*, 2000] allowing a more accurate simulation of ice crystal mixtures deduced from local in situ observations.

[9] With the latest improvements in the computation of ice crystal optical properties, the number of possible optical characteristics for space-borne retrieval is unlimited. Never-

theless, no single ensemble of microphysical characteristics chosen a-priori could begin to effectively account for the entire spectrum of cirrus cloud microphysical properties. To cover a representative range, however, model particle shapes were selected following these subjective criteria: (1) optical properties used in previous or current space-borne retrieval to allow for future comparisons, (2) optical properties including the different types of ice crystals collected with in situ observations (e.g., contrails and frontal cirrus clouds), and (3) optical properties including the extreme behavior of scattering phase functions in the range of scattering angles considered in the current remote sensing application ( $90^\circ < \Theta < 180^\circ$ ).

[10] Those criteria led to the selection of 14 different sets of optical properties:

1. Eight correspond to prescribed size distributions and mixes of different shapes. Of these, three correspond to the two extremes and the middle behavior of the different sets currently used in the Clouds and Earth's Radiant Energy System (CERES) cirrus cloud retrieval [*Minnis et al.*, 1998]; three others correspond to the two extremes and the middle behaviors currently used in the Moderate Resolution Imaging Spectroradiometer (MODIS) cirrus cloud retrieval; one is for ice crystals with a rough surface [*Yang et al.*, 2000]; and the last one is the polycrystal used by the International Satellite Cloud Climatology Project (ISCCP [*Rossow and Schiffer*, 1999]) for ice cloud optical properties.

2. Four correspond to monocrystals from *Macke et al.* [1996a] for a given particle size large compared to the wavelength.

3. Two correspond to liquid water spheres.

[11] The properties for each set of model shapes are summarized in Table 1 and examples of their scattering phase functions are plotted in Figure 1. At the wavelength of interest (0.65  $\mu\text{m}$ ), the particle size plays a minor role and only weakly influences the scattering phase function of the crystals in the angles of scattering used for the current retrieval ( $80^\circ$ – $180^\circ$ ). Hence, the following sensitivity study and application will mainly be for determination of cloud effective particle shape. The term “effective shape” is used here because the parameter of interest is a shape or combination of shapes that has a scattering phase function that best produces the observed radiances. Other shapes or combinations of sizes and shapes may produce the same

effect, but, for the sake of simplicity, the effect is referenced to one of the assumed microphysical models above.

## 2.2. Radiative Transfer Computations

[12] To account for cloud multiple scattering effects, as well as the effect of Rayleigh scattering and surface albedo, the ice crystal optical properties are used in the adding-doubling code of *De Haan et al.* [1986] to compute top-of-atmosphere (TOA) reflectances. The atmosphere is divided into three different homogeneous layers: the cirrus cloud layer, and the above- and below-cloud atmosphere layers composed exclusively of molecules. The surface albedo is taken into account as a limiting condition at the ground.

[13] The bidirectional reflectance was derived for various values of optical thickness for each of the cirrus types using several solar zenith angles  $\theta_s$  between  $20^\circ$  and  $60^\circ$ . The lower limit ( $20^\circ$ ) corresponds to the minimum value observed most frequently by satellites, while the upper value ( $60^\circ$ ) roughly corresponds to the limit of confidence in plane-parallel radiative transfer computations. The computations were performed at  $0.65 \mu\text{m}$ , a wavelength common to most satellite imagers. The TOA reflectance is only weakly influenced by Rayleigh scattering at this wavelength (that is, the cloud altitude will not have a significant impact on the computed radiances). The TOA reflectances were computed for eight different scattering angles selected based on the range of satellite viewing directions. To simulate the Triana views, scattering angles  $\Theta_T$  of  $175^\circ$  and  $168^\circ$  are considered, while for the LEO and GEO satellites, the range of most frequently occurring scattering angles [*Minnis et al.*, 1998] is covered by using  $\Theta_2 = 60^\circ, 90^\circ, 105^\circ, 120^\circ, 140^\circ, 150^\circ,$  and  $160^\circ$  in the computations, where the subscript 2 refers to the second satellite in the Triana-LEO/GEO pair.

## 2.3. Results

[14] The results are plotted as reflectance in a given direction ( $\Theta_2$  ranging between  $90$  and  $160^\circ$ ) as a function of the reflectance at  $\Theta_T$ . This representation has the advantage of being independent of the cloud optical depth, which is an unknown variable for this remote sensing study. The results shown in Figures 2–6 are for cirrus clouds located between 9 and 11 km above a Lambertian surface with an albedo  $\alpha_s = 0.03$  (ocean), composed of different types of ice crystals or water droplets, and observed at five different scattering angles. The dual-angle reflectances at  $\theta_o = 40^\circ$  are shown in Figure 2 for the models corresponding to the different effective particle sizes in the CERES, MODIS, and water droplet distributions. Except for  $\Theta_2 = 60^\circ$ , the three CERES reflectance curves show some slight separation due to effective particle size and the particular combinations of hexagonal column aspect ratios used to construct the various size distributions. Overall, the separation between these curves is less than that seen between the CERES models and the other shapes except for  $\Theta_2 = 60^\circ$  and  $150^\circ$ . The three MODIS results are also slightly separated for similar reasons, but are more distinct from the other curves than from each other. It is clear that most of the separation between the various models is due to crystal shape and secondarily to effective size. For clarity, only the middle MODIS and CERES curves are plotted hereafter, and the

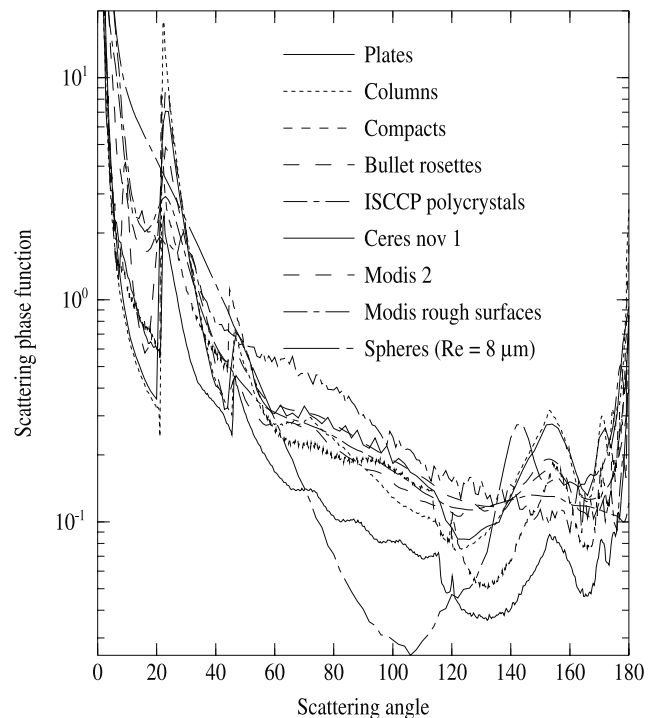


**Figure 1.** Scattering phase functions of the 14 different ice crystal types selected for shape retrievals.

monocrystals (columns, plates, bullet-rosettes and compacts) are discussed in the text (not plotted).

[15] Figure 3 shows the dual-angle reflectance diagrams for all of the models at  $\theta_o = 20^\circ$ . Figures 4 and 5 show the same plots for  $\theta_o = 40^\circ$  and  $60^\circ$ , respectively. Figures 2–6 show that the dual-angle reflectance curves for ice crystals are distinct from those for liquid water droplets for all viewing directions, except at two angles. At  $\Theta_2 = 60^\circ$  and  $140^\circ$ , the Mie scattering phase function crosses the ice curves (Figure 1); the latter angle corresponds to the rainbow peak. Reflectances from the other directions are potentially useful for discriminating the cloud thermodynamical phase. Moreover, at  $\Theta_2 < 150^\circ$ , the curves are sensitive to ice crystal shape. As  $\Theta$  decreases, the separation between the curves for the different shapes increases. The various monocrystal curves cover the largest range of values.

[16] Because the different scattering phase functions are strongly variable close to the backscattering direction, some of the same plots have been constructed for another Triana scattering angle,  $\Theta_T = 168^\circ$ , in Figure 6. The curves show the same tendency as those at  $175^\circ$  but with slightly less distinction between the different ice crystal types. At  $\Theta = 150^\circ$ , the phase function values are similar to those at  $168^\circ$  and  $175^\circ$  for most of the ice crystal models. Thus, there is minimal information about particle shape when  $\Theta_2 = 150^\circ$ . Values of  $\Theta_2$  between  $160^\circ$  and  $165^\circ$  would be more useful than those between  $150^\circ$  and  $160^\circ$ . Because of those phase function similarities,  $150^\circ$  could also serve as  $\Theta_2$  for pairs of angles that include  $\Theta_2 < 140^\circ$ . Calculations of reflectances for all pairs of angles between  $60^\circ$  and  $150^\circ$  (not shown) demonstrated that  $\Theta_T = 150^\circ$  is second only to  $\Theta_1$  between  $165^\circ$  and  $180^\circ$  for distinguishing particle shapes. Thus, the use of the Triana scattering angles for dual-angle viewing

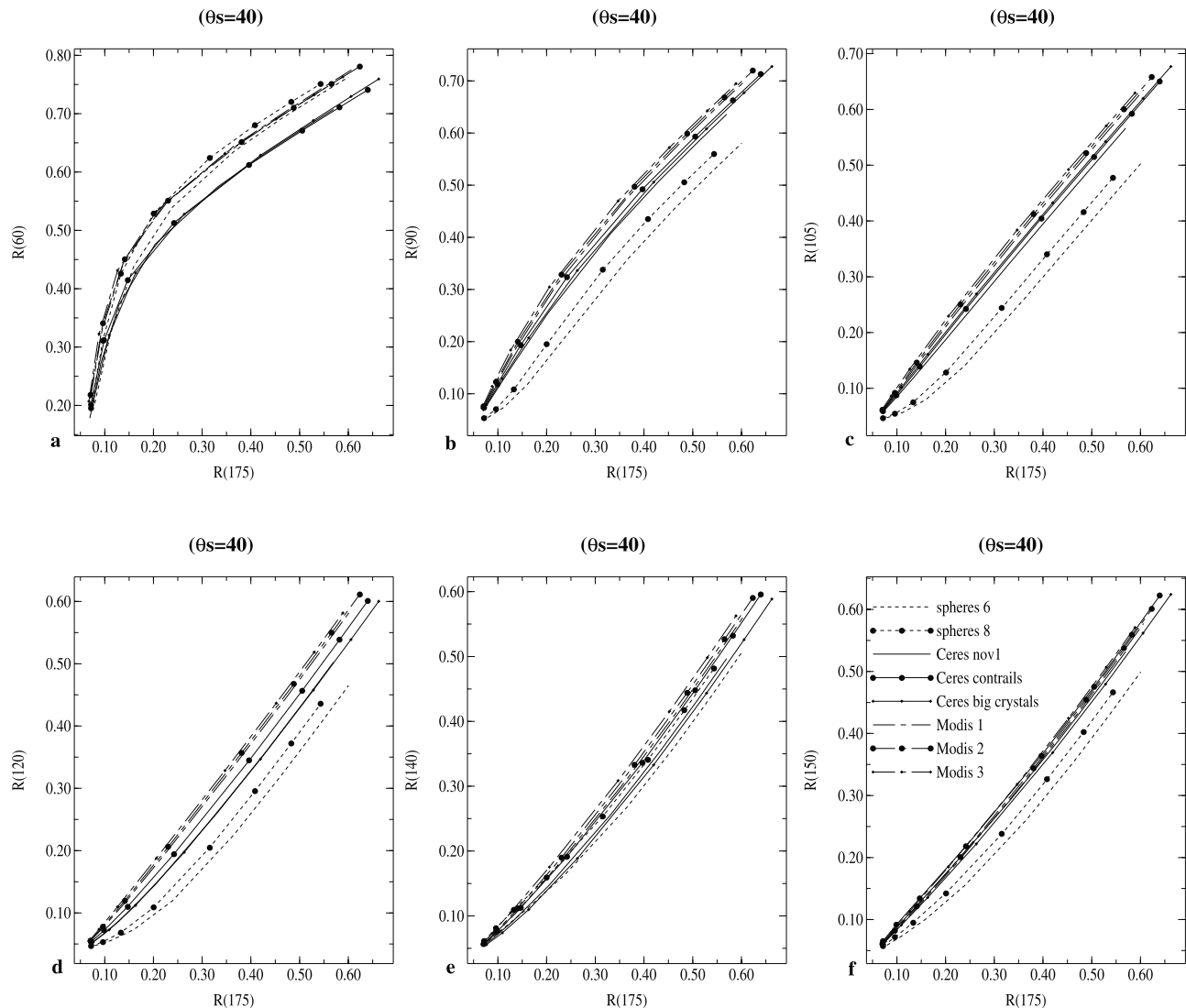


**Figure 2.** Simulations of reflectances for pairs of scattering angles using 3 ceres, 3 modis, and 2 sphere models.

should most often provide the optimal conditions for determining ice crystal shapes.

[17] Figure 7 shows examples of similar computations for a cirrus cloud composed of one particle type, polycrystals, over different surface types: sea ( $\alpha_s = 0.03$ ), land ( $\alpha_s = 0.15$ ), and desert ( $\alpha_s = 0.30$ ). Similar computations performed for various solar zenith angles showed that the surface albedo influences the reflectance curve more for thin clouds at low solar zenith angles and low scattering angles ( $\Theta < 100^\circ$ ). The influence of surface albedo on the separation of the reflectance curves can be neglected when the reflectance exceeds 50%. Otherwise, the bidirectional reflectance characteristics of the underlying surface must be taken into account.

[18] The impact of multilayer clouds was studied following the same method and revealed that the behavior of the reflectance curves is modified only when a thin cirrus cloud ( $\tau < 2$ ) is located above a thick low-level cloud. When  $\tau$  exceeds 2 for the upper cloud, the relative behavior of the curve is negligibly influenced by the lower cloud. Because

of this it may be concluded that the retrieved shape only corresponds to particles with the layer between the top of the cloud down to an optical depth of 2 or so.

[19] From the results in Figures 2–6 and from other computations, it is concluded that the remote sensing of ice crystal shape with the current method will be most effective in the following situations: (1) high values of  $\Theta_T$  (closer to  $177^\circ$  rather than  $165^\circ$ ), (2) low scattering angle ( $\Theta_2 < 150^\circ$ ) from the complementary satellite, and (3) high values of solar zenith angle. To simplify the comparisons and discussion, the 14 scattering phase functions are grouped in four different classes. (1) Class A includes the scattering phase functions corresponding to the upper level of curves on the reflectance diagram: isccp, modis\_rough, and plates. (2) Class B includes upper midlevel curves: modis\_1, modis\_2, modis\_3, and bullet-rosettes. (3) Class C includes low midlevel curves: ceres\_nov, ceres\_contrails, ceres\_big, columns and compacts. (4) Class D includes low-level curves: the two liquid water phase functions spheres\_6 and spheres\_8. It is assumed that the reflectance curves

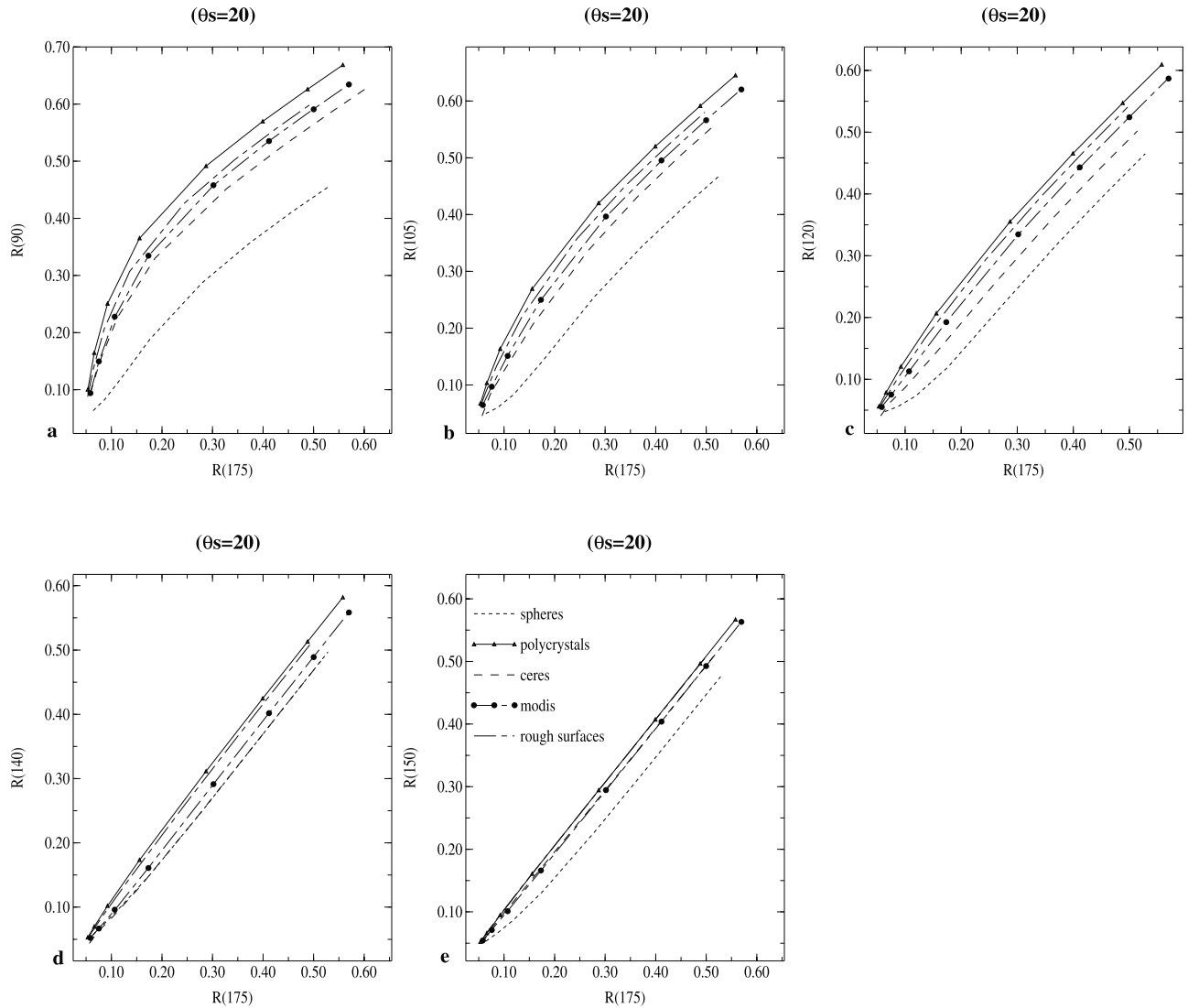


**Figure 3.** Reflectance at a given scattering angle  $\Theta_2$  as a function of reflectance at  $\Theta_T = 175^\circ$  for different cirrus cloud microphysical characteristics over a sea surface for  $\Theta_2$  values of (a)  $60^\circ$ , (b)  $90^\circ$ , (c)  $105^\circ$  (d)  $120^\circ$ , and (e)  $150^\circ$ , with  $\theta_s = 20^\circ$ .

within each of these classes are similar enough such that one of the models in the class can represent the others.

### 3. Case Studies

#### 3.1. Data Set

[20] To test the capability of determining cirrus particle shape by combining Triana data with other satellite imagery, several cases of satellite observations with the proper viewing and illumination angles were developed for comparison with the simulations. First, visible data from a satellite viewing a scene containing extensive cirrus clouds with  $\Theta$  between  $165$  and  $178^\circ$  is selected, then matched with coincident data from another satellite. This procedure is most easily accomplished by using at least one GEO satellite with any other coincident satellite. Here, the eastern Geostationary Operational Environmental Satellite (GOES-8 or G8) always provides one view while the GOES-10 (G10) at  $135^\circ\text{W}$ , the NOAA-14 Advanced Very High Resolution Radiometer

(AVHRR), and the Visible InfraRed Scanner (VIRS) on the Tropical Rainfall Measuring Mission (TRMM) satellite provide the matching views for a variety of cases.

[21] The visible channel on each of the satellite imagers was normalized to the G8 visible channel following the procedures of *Nguyen et al.* [1999]. Briefly, mean visible brightness counts or radiances were computed for  $0.5^\circ$  latitude-longitude boxes from each satellite data set for areas that were viewed by both satellites within a few minutes of each other at nearly the same angles. The GOES visible (VIS) channel ( $0.65 \mu\text{m}$ ) data are usually provided in 10-bit counts (CNT) while the VIRS and AVHRR VIS data are given in radiance. In the normalization procedure, the radiances are converted to GOES-equivalent radiances  $L_G$  by multiplying the observed radiance by the ratio of  $526.9 \text{ Wm}^{-2} \mu\text{m}^{-1}$  to the solar constant of the particular satellite. A linear regression fit is then computed forcing the radiance to zero at the space count of the GOES. For both G8 and G10, the nominal space count is 28.5. Figure 8 shows the

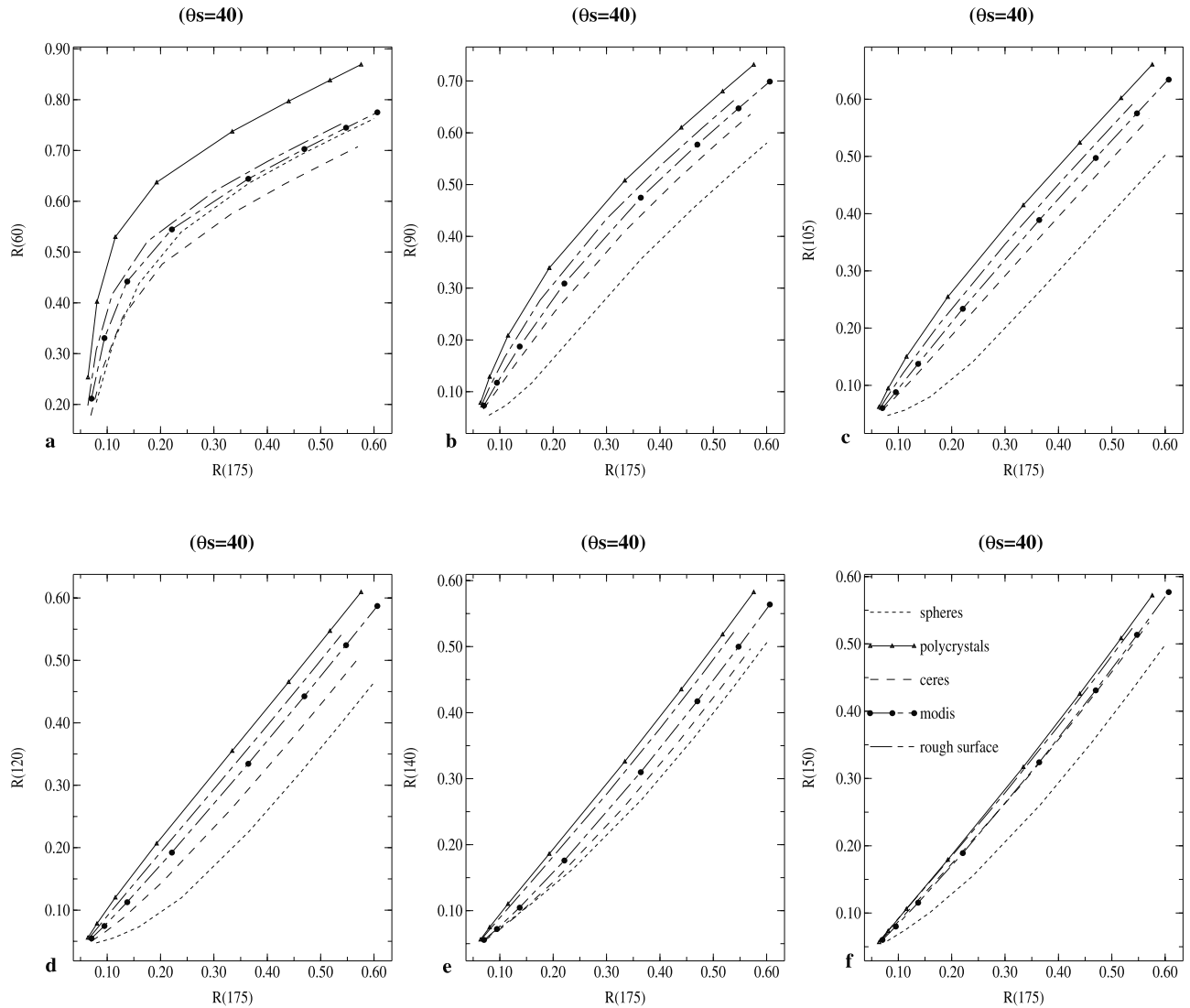


**Figure 4.** Same as Figure 2, except for  $\theta_s = 40^\circ$ .

scatterplots and resulting linear fits used to normalize G8 to VIRS and G10 to G8 for matched data taken during October 1999. For Figure 8a,

$$L_G = 0.8934 \text{ CNT}_{G8} - 25.5,$$

and for Figure 8b,

$$L_G = 0.6426 \text{ CNT}_{G10} - 18.6.$$

The standard estimates of the errors (SE) in these fits are 6 and 8%, respectively. Similar normalizations were performed for the remaining cases. The SE varied from 6 to 12% overall. The uncertainties in the fits are 1.6 and 1.0%, respectively. The relative calibration of the two instruments is most important here as an error in the curves will produce a bias. Thus, the uncertainties in the fits provide the best estimate for assessing the impact of the intercalibration on the retrievals.

[22] The radiance for a given pixel is then used to compute the reflectance,

$$\rho = L_G / 526.9 \mu_o \delta,$$

where  $\delta$  is the Earth-Sun distance correction factor and  $\mu_o$  is  $\cos \theta_o$ .

[23] The reflectance data set for comparing with model calculations like those in Figures 2–6 was constructed from these normalized reflectance data using the following procedures and constraints. (1) Two satellite images are collocated in space and time with time differences less than 15 min. (2) One satellite image has some Triana viewing geometry ( $165 < \Theta < 177^\circ$ ). (3) For each of the two images, the means and standard deviations of  $\rho$  and infrared ( $11 \mu\text{m}$ ) temperatures  $T$  are computed for each grid box in a  $0.25^\circ \times 0.25^\circ$  (or  $0.5^\circ \times 0.5^\circ$ ) latitude-longitude grid over the domain containing the Triana scattering angles. (4) Some of the grid boxes contain only ice clouds ( $T < 240 \text{ K}$ ). (5) Only the grid boxes containing more than 20 pixels for each image with reflectance and temperature standard deviations less than 10% are considered, in order to reject strongly inhomogeneous clouds. (6) For a given image pair, the cloud area is divided in several subareas corresponding to a  $5^\circ$  range in  $\theta_o$ ,  $\theta$ , and relative azimuth angle, in order to assume constant angles and constant surface albedo in the simulation calculations for the subarea.

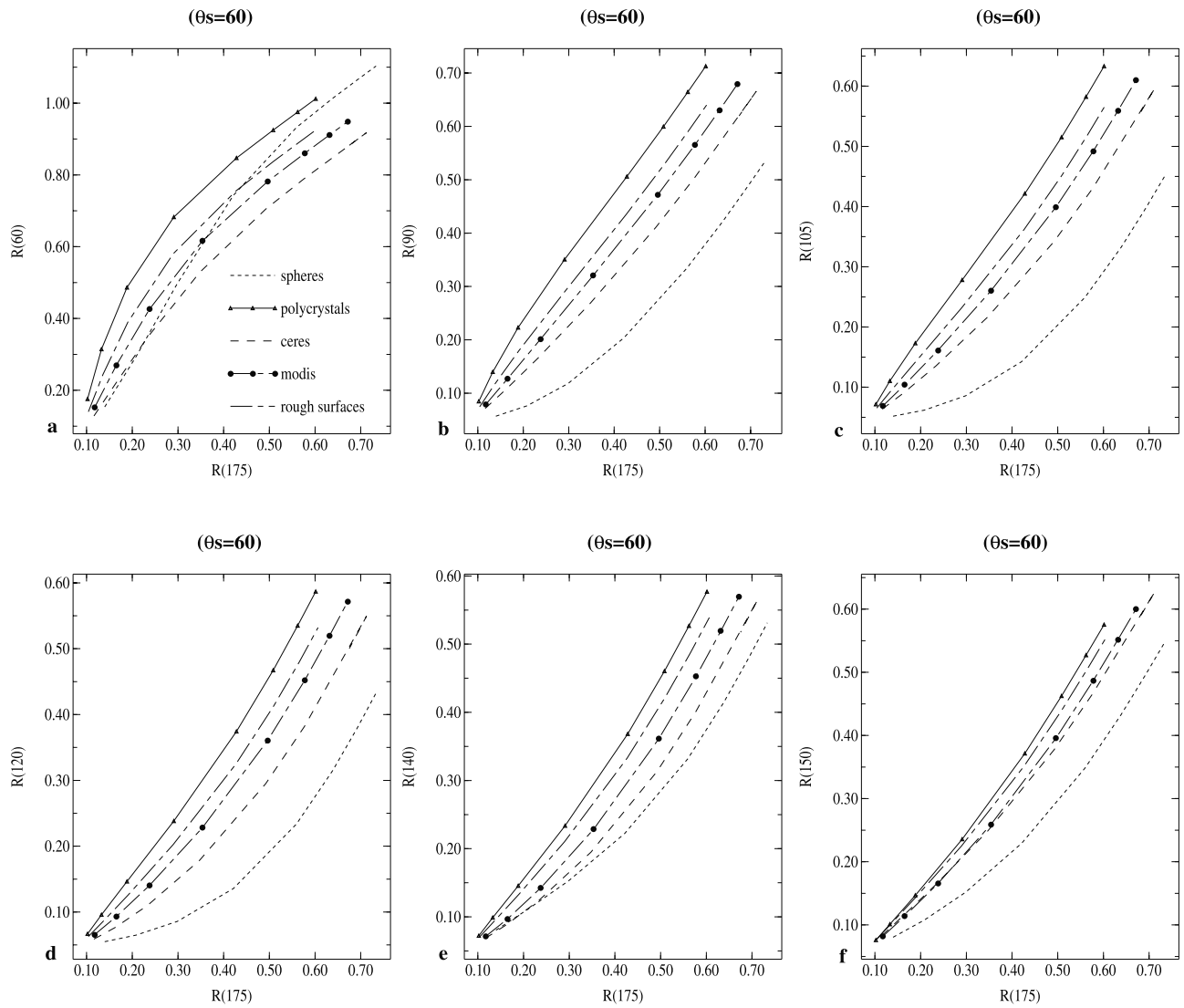


Figure 5. Same as Figure 2, except for  $\theta_s = 60^\circ$ .

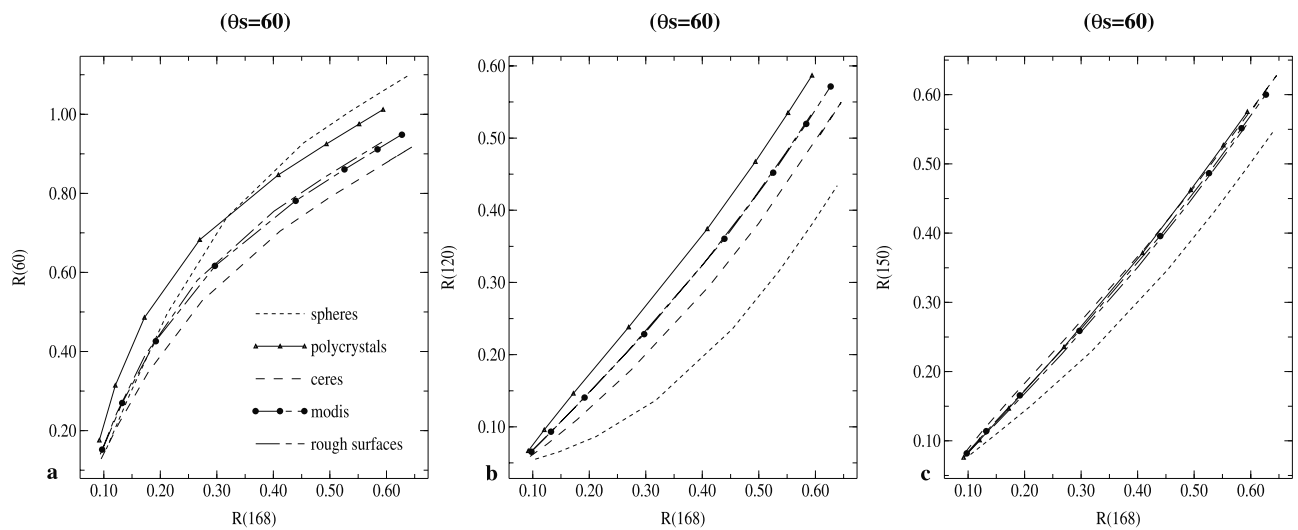
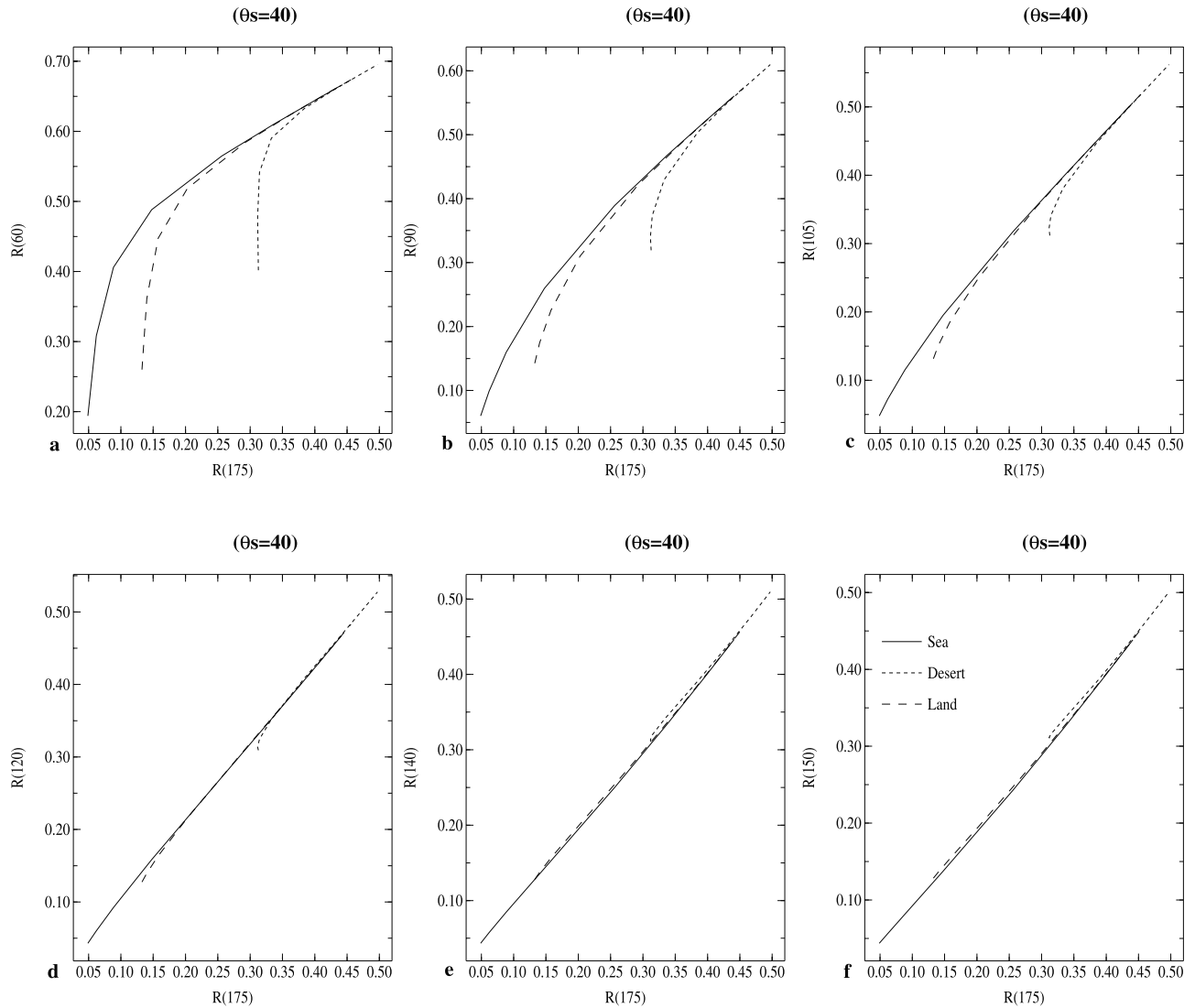


Figure 6. Same as Figure 5, except for  $\Theta_T = 168^\circ$ , and  $\Theta_2$  values for (a)  $60^\circ$ , (b)  $120^\circ$ , and (c)  $150^\circ$ .



**Figure 7.** Same as Figure 2, except for a cirrus cloud composed of polycrystals over a range of surface albedos.

[24] The uncertainty in the relative calibrations is assumed to be the error in the linear fits which is less than 2%. The different cases, summarized in Table 2, include cirrus and liquid water clouds observed above the central United States, the western North Atlantic, the Caribbean Sea, and the eastern North Pacific, with  $\theta_0$  varying between  $20^\circ$  and  $70^\circ$ .

### 3.2. Results

[25] Figures 9 and 10 show the imagery, angles, and reflectance ratios for two cases listed in Table 2. In Figure 9, a low-pressure system centered over Oklahoma during 31 October 1999 contains a core with ice (see colder clouds in the IR image) surrounded by water clouds except on the eastern side of the image. The G8 (GOES East) scattering angles vary from  $167^\circ$  to  $171^\circ$  while the G10 (GOES West) angles range from  $119^\circ$  to  $122^\circ$ . G10 measures smaller reflectances than G8 over all scenes except for some of the cold clouds. The reflectance ratios for the water clouds are generally between 0.80 and 0.90 and exceed 0.90 for the ice clouds with the greatest values on the eastern edges of the

cirrus clouds. Thus, some difference between the ice and water clouds is clearly evident in the ratio imagery. Figure 10 shows another storm system over the central United States during 11 March 2000. The G8 scattering angles are between

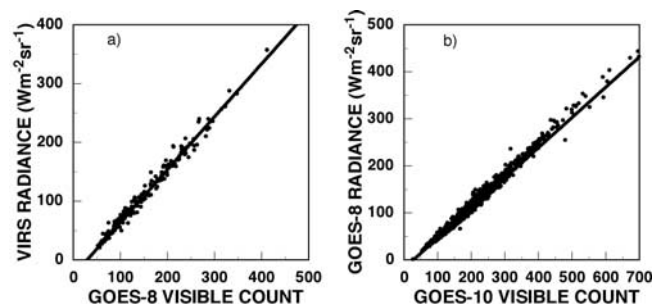


**Figure 8.** Scatterplot and linear regression fit of (a) G8 counts and VIRS radiance and (b) G10 counts and G8 radiance for matched fields of view over ocean during October 1999.

**Table 2.** Cases Studied<sup>a</sup>

Date, dd mm yy	Time, UTC	$\theta_s$	Location	View 1 $\theta \psi \Theta$	View 2 $\theta \psi \Theta$
<i>G8/VIRS (Time Difference = 9 min)</i>					
01 10 99*	1650	20	18°N–80°W Caribbean Sea	20 178 179	20 150 170
<i>G8/NOAA (Maximum Time Difference = 15 min)</i>					
27 08 00	2050	63.5–66	33°N–66°W Atlantic Ocean	40 111 124	52 178 166
05 09 00*	2055	66.5–70	27°N–65°W Atlantic Ocean	33 118 124	60 177 169
<i>G10/G8 (Maximum Time Difference = 2 min)</i>					
31 10 99*	1700	52.5	36°N–96°W Oklahoma, USA	58 106 119	47 167 169
10 03 00	1630	47.5	35°N–95°W Oklahoma, USA	59 80 104	46 170 173
	1700	43.5		59 90 110	16 179 178
	1730	40.5		59 102 119	46 170 173
11 03 00*	1600	52	40°N–89°W Illinois, USA	65 80 98	48 161 165
	1630	48		66 89 103	48 169 171
	1700	45.5		66 98 111	48 179 176
	1730	44		66 109 119	48 171 172
12 03 00	1600	57	43°N–94°W Iowa, USA	64 83 98	54 163 165
	1630	53		64 90 104	53 170 171
	1700	49.5		64 99 111	53 179 176
	1730	47		65 109 119	53 172 172
13 03 00	1600	56.5	34°N–104°W New Mexico, USA	52 73 98	50 165 166
	1700	46.5		53 88 108	50 180 173
	1730	42.5		53 97 114	50 171 170
14 03 00	1600	50	31°N–96°W Texas, USA	55 68 97	46 163 166
	1630	45		56 75 101	75 171 170
	1700	40		5784 106	43 179 173
	1730	36.5		55 96 115	43 170 170
<i>G10/G8 (Maximum Time Difference = 15 min)</i>					
26 08 00*	1622	40–45	8°N–108°W Pacific Ocean	33 11 107	40 162 167
	1652	33–37		32 10 115	40 162 169
27 08 00	1622	37–41	8°N–104°W Pacific Ocean	37 12 107	36 160 167
	1652	29–33		37 13 114	36 161 169
28 08 00	1622	36.5–40	12°N–97°W Pacific Ocean	39 24 107	37 159 167
	1652	30.5–34		36 17 114	38 162 169

<sup>a</sup>Angles are given in degrees. Asterisks indicate cases presented in figures.  $\theta_s$  corresponds to the solar zenith angle  $\theta$ ,  $\psi$  correspond to the zenithal and azimuth viewing angles, and  $\Theta$  is the scattering angle.

177° and 179° while those for G10 are between 111° and 114°. The colder ice clouds are northeast of the warmer water clouds. Again the reflectance ratios are generally less than 0.9 for the warmer clouds and between 0.9 and 1.2 for the colder clouds.

[26] The results for the 31 October 1999 case (Figure 9) are plotted in Figure 11. All of the data for the warmer clouds fall close to the water droplet reflectance curve, while most of the points for the colder clouds lie between the CERES and MODIS curves. The scatter in the ice crystal points, corresponding to the wide range of reflectance ratios in Figure 9, is considerable, perhaps, reflecting substantial variability in the types of crystals at cloud top. Cloud phase differences are very distinct, however.

[27] Figure 12 shows the results obtained for 11 March 2000 at 1600 UTC (Figure 12a), 1630 UTC (Figure 12b), 1700 UTC (Figure 12c; see Figure 10) and 1730 UTC (Figure 12d). To a first approximation, these plots can be considered as a picture of the microphysical evolution of these clouds. In all cases, the warmest pixels are closest to the water droplet curves, while the colder pixels have significant scatter for a given G8 reflectance. At 1600 UTC, the mixed ( $T$  between 240 and 258 K) and cold ( $T < 240$  K) pixels are between class D and class C (mixtures of water spheres and columns), then mostly line up with the class C (CERES and column) models by 1630 UTC. By 1700 UTC, the colder pixels are centered more on the class

B (bullet rosettes and MODIS) than on the class C models. At 1730 UTC, the points are closest to the bullet rosette and compact curves (not shown), suggesting a mixture of classes B and C. Although the cloud system moved during the hour and half, the observations mostly include the same cloud parcels, so that the changes in dominant crystal type seen in Figure 12 may reflect the dynamical evolution of the cloud.

[28] Figure 13a shows the results of the comparisons between the G8/VIRS observations and the simulations for 1 October 1999. All of the selected pixels correspond to ice cloud ( $T < 240$  K). Both observed scattering angles, 169° and 178°, are close to the backscatter direction, but correspond to substantial differences in most of the phase functions thus leading to a large separation between the different computed reflectance curves. The vertical scatter is negligible compared to that seen in Figures 11 and 12. For this case, the model corresponding to modis\_rough (class A) ice clouds is best suited to explain the observations. Figure 13b, corresponding to 5 September 1999, shows that the CERES models explain these observations better than the other models.

[29] Ten additional cases were analyzed following the same method used for Figures 11–13. A first attempt to classify the different results obtained for the cases studied is summarized in Table 3. In Table 3, the best fit (or fits) to the observations is given when it can be clearly determined.

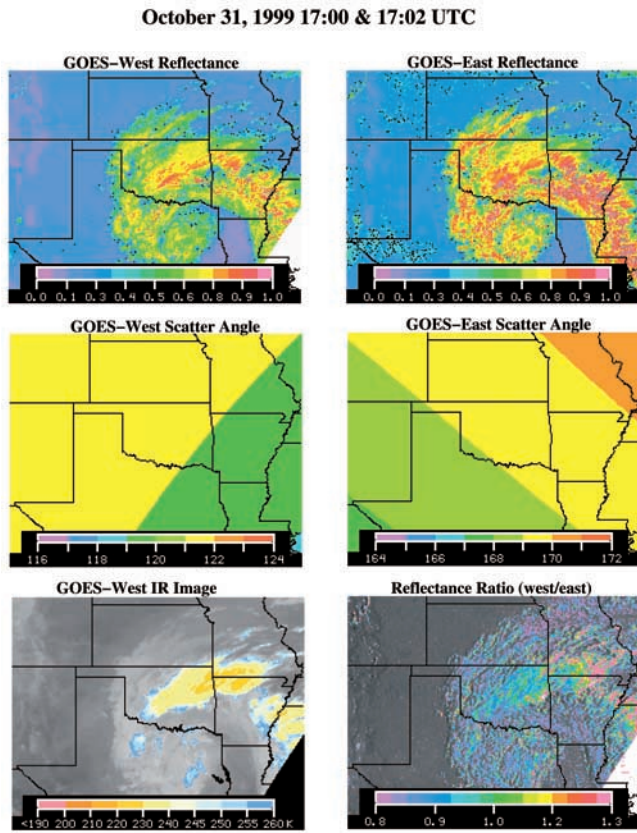


**Figure 9.** Imagery, scattering angles, and reflectance ratios for G8 and G10 data used in 1700 UTC, 31 October 1999 case.

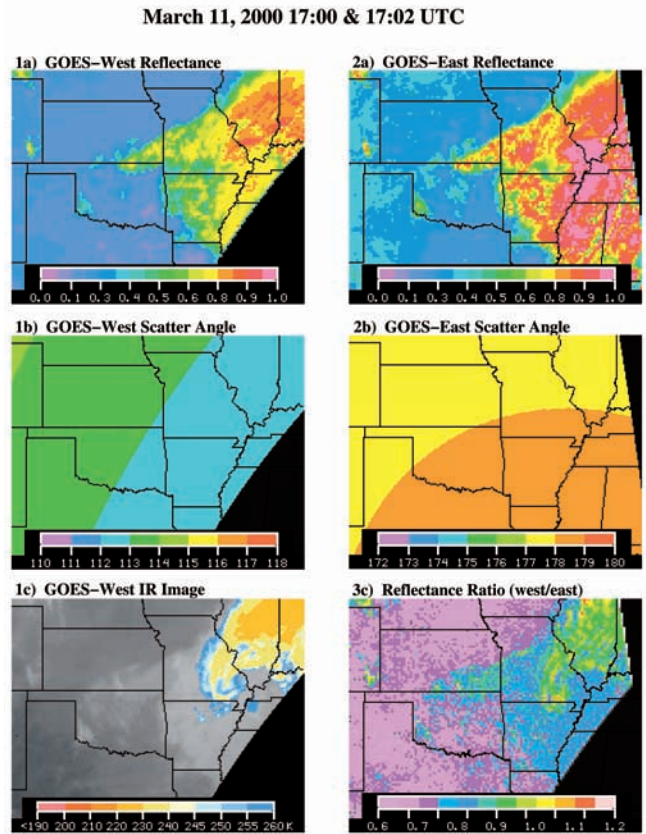


**Figure 10.** Same as Figure 9 except for 1700 UTC, 11 March 2000 case.

When no simulations clearly fit data, the two microphysical models surrounding the data are selected because a mix of different ice crystal types (see Figure 11) may be responsible for the scatter. The reflectance levels are also indicated in Table 1. Most of the clouds were optically thick because of the high reflectance levels that were encountered. Of the 28 cloud systems, 71% were predominantly Class B and/or C, 39% included significant amounts of Class A, and 14% had mostly class D crystals or droplets. Cloud reflectances were mostly above 45%, except for 13 March when they ranged between 30 and 45%.

[30] Except for 3 March, all of the multi-image cases during March 2000 show a very consistent progression of ice crystal shapes from 1600 through 1730 UTC. A mixture of water droplets and columns dominate at the earliest time, followed by a combination of the Class C (CERES) and B (MODIS) models, and, finally, by mixtures of class A and B ice crystals. The 3 March sequence differed only at 1730 UTC when no class A crystals were observed. The five tropical Pacific results showed no dominant class of crystal shape except for the 28 August 2000 case, which revealed few Class A shapes. Class B and C models were found most often for the two subtropical Atlantic cases.

#### 4. Discussion

[31] The ice crystal shapes found in these case studies further demonstrate that the ice crystal types in cirrus clouds

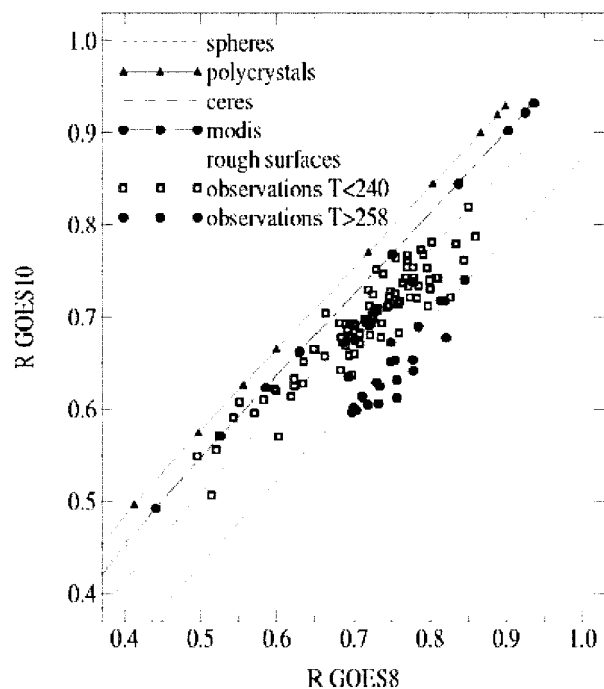


**Figure 11.** Comparisons between simulations and G8-G10 observations for 1700 UTC, 31 October 1999.

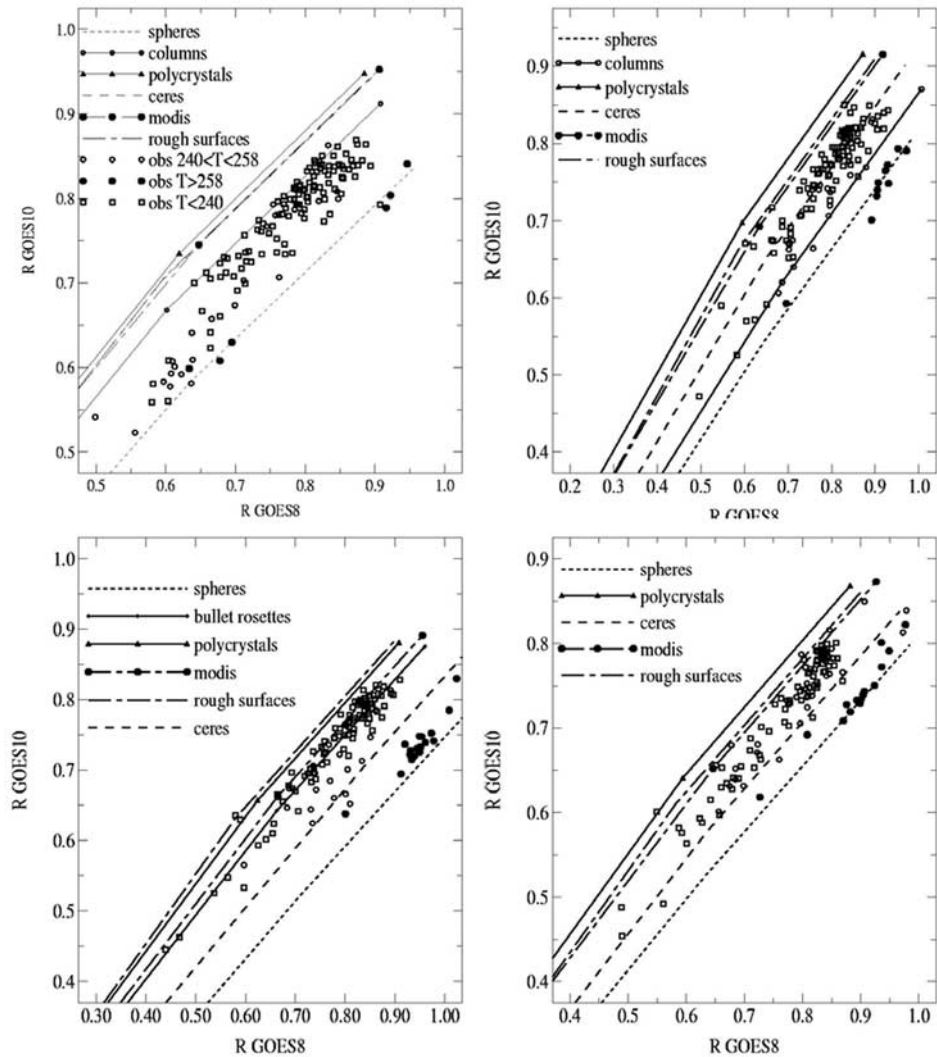


**Figure 12.** Comparisons between simulations and G8–G10 observations for 11 March 2000 at (a) 1600, (b) 1630, (c) 1700, and (d) 1730 UTC.

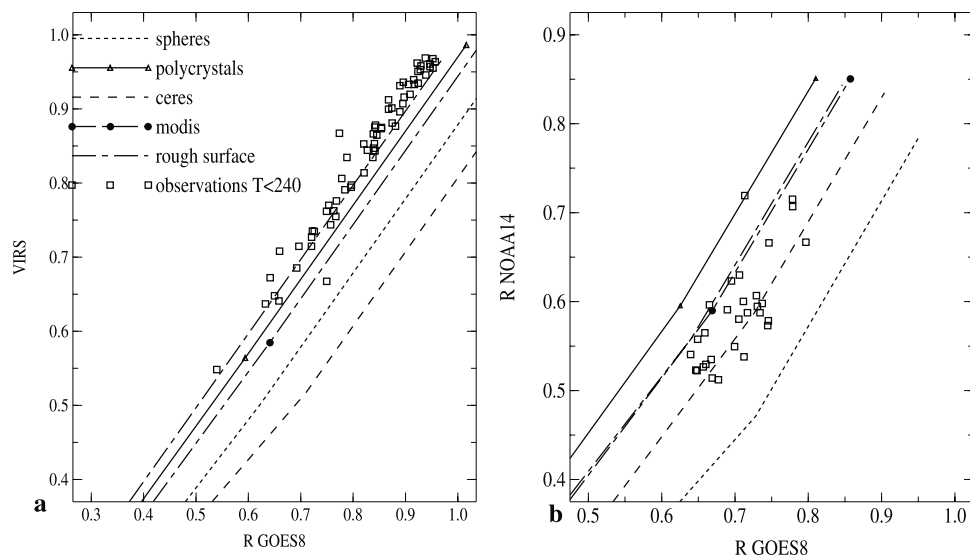


**Figure 13.** Comparisons between simulations and observations collected with (a) G8 and VIRS taken at 1650 UTC, 1 October 1999 and (b) G8 and NOAA-14 from 5 September 2000.

**Table 3.** Summary of Case Study Results

Date, dd mm yy	Time, UTC	Class				Reflectance Level, %			
		A	B	C	D	30–45	45–60	60–75	75–90
01 10 99	1645 <sup>a</sup>	o						x	x
31 10 99	1700			o				x	
10 03 00	1630			o					x
	1700			o				x	x
	1730			o				x	x
	1730	o	o				x		
11 03 00	1600 <sup>a</sup>			o	o			x	x
	1630 <sup>a</sup>			o				x	x
	1700 <sup>a</sup>			o				x	
	1730 <sup>a</sup>			o	o			x	
12 03 00	1600			o	o			x	x
	1630			o	o			x	x
	1700			o	o			x	x
	1730	o						x	x
13 03 00	1600		o	o			x		
	1700		o	o			x		
	1730		o	o			x		
14 03 00	1600			o	o			x	x
	1630			o	o			x	x
	1630	o	o					x	
	1700	o	o					x	x
	1730	o	o					x	x
26 08 00	1622	o	o	o					x
	1652	o	o	o					x
27 08 00	1622	o	o	o					x
	1652 <sup>a</sup>	o	o	o					x
27 08 00	2050	o	o	o				x	x
28 08 00	1652		o	o					x
05 09 00	2055 <sup>a</sup>		o	o				x	x

<sup>a</sup>Cases presented in figures.

are highly variable. From these results, it can be concluded that the use of a single model or set of models without explicit identification of the shape can lead to significant errors in optical depth retrieval from a single measured reflectance value. Although not conclusive because of the small sample, it appears that use of either the CERES or MODIS models will result in similar levels of uncertainty with minimal bias, on average. Because they are comple-

mentary, however, the resulting biases should be opposite in sign. The use of models closer to the extremes of those considered here (e.g., water droplets and class A) will probably yield more biased optical depths in the mean. Many more cases should be analyzed before arriving at any firm conclusions about the statistical representativeness of any of the models because only a few thick systems and no thin cirrus were examined.

#### 4.1. Uncertainties

[32] It can be concluded, however, that the proposed dual-angle approach proposed can be used to determine cloud-top phase and retrieve effective cloud particle shape although the scatter in the data around the reflectance curves suggests that such an approach may yield relatively uncertain results. However, other studies using in situ or remotely sensed data have documented the highly variable nature of cirrus microphysical properties [e.g., *Heymsfield, 1993; Spinhirne et al., 1996*]. Thus, the variability of ice crystal shape suggested by most of the results in Table 3 may be the norm for cirrus clouds, while the homogeneity apparent in Figure 13 may be atypical. Despite the expectation of a wide range of results over a large cloud system, there are a number of other sources of uncertainty that should be considered.

[33] The relative calibrations of the two satellites will not contribute to the scatter, but will shift all of the data points in one direction relative to the computed curves. For the present study, the calibration uncertainty is less than 2%. It corresponds typically to the size of the squares used to plot observations in Figures 11–14, so this uncertainty will still allow discrimination between the four different classes of particles (A, B, C, and D). Thus, the calibration uncertainty would not introduce large errors in particle shape for most of the angular configurations. Random errors in the retrieval would be introduced primarily by temporal and spatial mismatches in the fields of view. Navigational errors and differences in pixel sizes and locations result in slightly different fields of view for each set of matched points. The degree of mismatch depends on the quality of the pixel

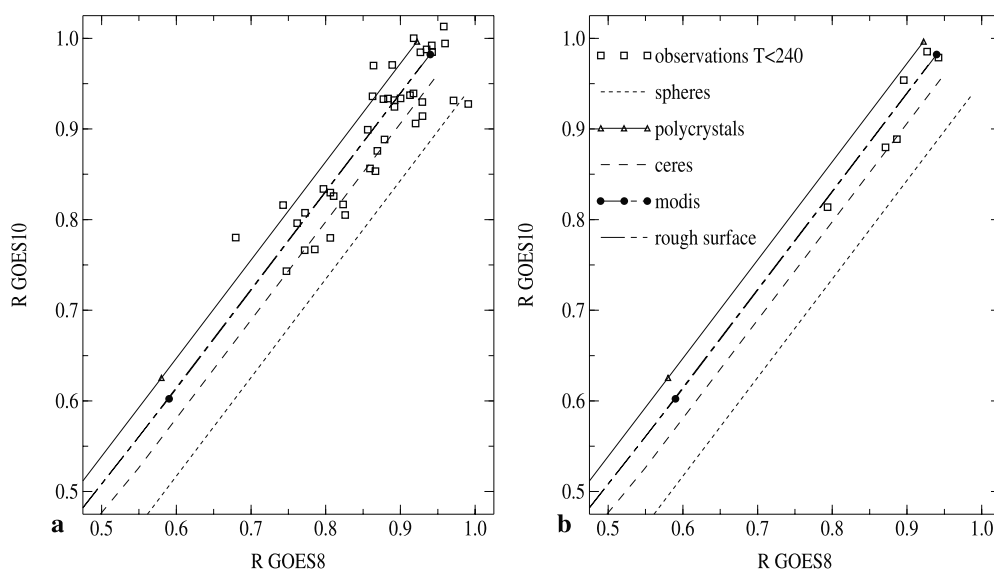


**Figure 14.** Comparisons between simulations and G8/G10 observations at 1652 UTC, 26 August 2000 for latitude-longitude grid boxes of (a) 0.25° and (b) 0.5°.

registration for each satellite and the size of the area (number of pixels) used for each data point. The navigation uncertainty in the planned Triana images should be around 2 km, similar to that for other satellite images. This uncertainty is small compared to the size of many cirrus clouds (hundreds of square kilometers) and should not significantly affect the shape retrieval, except at the cloud edges.

[34] A larger source of scatter in the results is the temporal mismatch. Because cirrus clouds often move at high speeds and may undergo significant changes in a short time, the time difference between the two images can be a critical factor for retrieving an accurate cloud particle shape. Time differences up to 15 min between the two satellites were used in several of the cases because it is likely that the EPIC will take an image at least every 30 min. Increasing the size of the averaging area for the matched data should reduce the noise introduced by cloud motion because a larger area decreases the proportion of mismatched area within the averaging region. For example, at a given wind speed of  $100 \text{ km h}^{-1}$ , half of the area would be mismatched for a  $50 \text{ km} \times 50 \text{ km}$  box compared to 100% for a  $25 \text{ km} \times 25 \text{ km}$  region. Figure 14 illustrates this point with data from G8 and G10 images taken 15 min apart on 26 August 2000. The mean reflectance pairs computed for  $0.25^\circ \times 0.25^\circ$  latitude-longitude boxes (Figure 14a) show a great deal of scatter with some points outside the range of the models while others appear to be water droplets. When averaged over a  $0.50^\circ \times 0.50^\circ$  box, the number of data points is reduced by more than a factor of 4 but the extreme points are eliminated. The new points either line up with the *ceres* curve or fall between the *modis* and *Isccp* reflectance curves. Thus, although the number of points is reduced for a given area, increasing the averaging area yields more realistic results. While increasing averaging area can reduce the scatter, it cannot account for changes in the particle shape during the time interval between images. As seen in Figure 12, the particle shapes appear to change rapidly in the course of only 30 min. To obtain a more complete accounting of the errors due to time differences in the images, it will be necessary to perform a more detailed study using a greater number of images taken in the midlatitudes and tropics where the wind speeds are often high and low, respectively.

[35] The radiative transfer computations used here assume a plane-parallel cloudy atmosphere, which is not always realistic. The cirrus cloud heterogeneities and structure can lead to a more scattered ensemble of points and, therefore, to a more uncertain retrieval of the particle shape. In those cases, the variance of the cloud temperature, as measured in the window channel by several of the GEO/LEO satellites can be used as a criterion to select the cloud with minimal horizontal inhomogeneities, which may limit the application of a plane-parallel approximation. Moreover, the impact of vertical inhomogeneities on bidirectional radiances at  $0.65 \mu\text{m}$  has been studied by *Yang et al.* [2001] in considering real vertical profiles of crystal shapes within the cirrus cloud: for optically thick clouds with an optical around 10, the radiance value is modified of less than 3% depending on the vertical structure; for thin cirrus clouds (optical depth of 1), this can reach a maximum of 5% for certain viewing scattering angles. Most of the cirrus clouds used in this study were optically thick and required little consideration of the back-

ground reflectance. Because many cirrus clouds are optically thin, it will be necessary to account for the anisotropy of the background reflectance to retrieve an accurate particle shape and to determine the sensitivity to the brightness of the underlying surface, which can be land, ocean, snow, or another cloud. The cases used here mostly included high altitude clouds, so any differences due to Rayleigh scattering are negligible. The errors introduced by not including ozone absorption are also negligible because the path lengths for the two views differ only by the  $\cos \theta$  differences, resulting in less than 1% error for all of the cases.

[36] The results in these case studies are very realistic in that the water droplet models fit the warm cloud data points closely and the other data points fall within the bounds given by the model curves, except for the data in Figure 14a. Some independent means of confirming the results will be needed to fully validate the retrievals. Either in situ or other remote sensing techniques are needed to verify these results. Additionally, only the particle shapes within the top portion of the cloud are retrieved with this and most other available techniques. Thus, it will be necessary to evaluate how well this retrieved shape represents the cloud overall. That assessment is critical for using this approach to derive cloud ice water path.

## 4.2. Implementation

[37] The dual-angle method for determining cloud particle shape could be implemented with any pair of collocated satellite images that are sufficiently contemporaneous. From the theoretical calculations, it is clear that use of one satellite that views near the backscattering direction and another viewing at  $\Theta < 150^\circ$  is the most efficient and accurate combination of images. Such complementary geometry is occasionally available with current operational and research satellites, but is not particularly consistent and provides limited sampling capabilities. Use of a satellite in L1 orbit, like Triana, as the backscattering satellite would be the most effective means for implementing this method. Thus, one scenario for implementing the technique using Triana with other satellites is outlined here.

[38] Pixels from a complementary satellite imager having a resolution of 4 km or better would first be analyzed with a selection of reflectance and emittance models representing a range of cloud particle shapes like those in Table 1 to derive optical depth and particle size (e.g., 9 [*Mace et al.*, 1998; *Minnis et al.*, 1999]). The results would then be used to predict the reflectance at the Triana view using the derived pair of particle size and optical depth for each shape. The anisotropy of surface reflectance, Rayleigh scattering, and atmospheric absorption would be taken into account when calculating the Triana-view reflectances. These reflectances would then be averaged to match the corresponding Triana field of view and compared with the reflectance observed from Triana. The closest match would then be selected as the particle shape. In this or a similar fashion, it should be possible to obtain both particle size and shape, and, subsequently, ice water path [e.g., *Minnis et al.*, 1998].

## 5. Concluding Remarks

[39] Cirrus cloud optical properties need to be better quantified at a global scale with the highest time and space

resolution possible to determine their global radiative impact and role in the hydrological cycle. This paper examined the potential of using the EPIC imager on the future Triana satellite coupled with other satellite observations to retrieve the ice crystal shape in cirrus clouds nearly continuously in time for the sunlit half of the Earth. This method is based on the sensitivity of the reflectance collected in two different directions to the ice crystal shapes. Those two directions will be observed simultaneously by Triana at scattering angles,  $165^{\circ}$ – $177^{\circ}$ , and by another LEO or GEO satellite in another direction. Based on a theoretical sensitivity study, it is shown that cloud thermodynamical phase can be deduced from such observations when the second satellite's scattering angle ranges between  $60^{\circ}$  and  $150^{\circ}$ , except at  $60^{\circ}$  and  $140^{\circ}$ . Moreover, the reflectance pairs corresponding to at least three different classes of effective ice crystal shape are distinct. The separation between the pairs is always possible if the second scattering angle is less than or equal to  $150^{\circ}$ , but it is more strongly marked for the greater values of the Triana scattering angle (e.g.,  $175^{\circ}$  rather than  $168^{\circ}$ ), and for high solar zenith angle (e.g.,  $50^{\circ}$  rather than  $20^{\circ}$ ).

[40] A simulated Triana data set was constructed using current in-flight satellite observations collected above the United States and adjacent marine areas. Cases from this data set were used to check the capability of the method for retrieving effective particle shape. In general, the models can account for the variation in the observed reflectance pairs, except when the time difference approached 15 min. In those cases, larger averaging areas eliminated the points that fall outside of the theoretical curves. Mixtures of columns, compacts, and bullet rosettes were the most common types of models matching the data points. The natural variability of cirrus cloud effective particle shapes is quite evident in the observation-model comparisons. Although not conclusive, the results indicate that the models currently used by CERES or MODIS for retrieving ice particle size are reasonable but not applicable to all cirrus clouds. However, a much larger sample of data points is needed to make any firm conclusions. A progression of changes in particle shape occurred over a 2-hour period in several midlatitude cyclone cloud systems. Additional validation is needed to determine if the cloud fields actually evolve in the observed manner.

[41] It is concluded that this approach has some potential for discriminating effective particle shape in cirrus clouds and can, at a minimum, be used to assess the errors introduced by assuming one particular particle model for retrieving cirrus cloud properties. However, if this technique is implemented using a combination of data from an L1 platform like Triana and a set of LEO and GEO satellites, it should be possible to obtain a nearly complete daytime survey of cloud particle shape/size, and, subsequently, estimates of ice water path for improved understanding and modeling of cirrus clouds.

[42] **Acknowledgments.** The authors are very grateful to Johan De Haan and Joop Hovenier for providing the doubling-adding code. Thanks are also due to Ping Yang and Andreas Macke for the ice cloud scattering phase functions for the bullet-rosette, MODIS, and ISCCP models. This research was supported by the CERES and Triana Projects as part of the NASA Earth Sciences Enterprise Program and was conducted while author Helene Chepfer was a visiting scientist at NASA Langley Research Center

under the sponsorship of the Institute for Computer Applications, Science, and Engineering in Hampton, Virginia.

## References

- Baran, A. J., S. J. Brown, J. S. Foot, and D. L. Mitchell, Retrieval of tropical cirrus thermal optical depth, crystal size and shape using a dual view instrument at  $3.7\ \mu\text{m}$  and  $10.8\ \mu\text{m}$ , *J. Atmos. Sci.*, **52**, 4246–4263, 1999.
- Chepfer, H., G. Brogniez, P. Goloub, F. M. Breon, and P. H. Flamant, Cloud ice crystals horizontally oriented in space observed with POLDER-1/ADEOS, *J. Quant. Spectrosc. Radiat. Transfer*, **63**, 521–543, 1999.
- Chepfer, H., P. Goloub, J. Riedi, J. De Haan, J. W. Hovenier, and P. H. Flamant, Ice crystal shapes in cirrus clouds derived from POLDER-1/ADEOS-1, *J. Geophys. Res.*, **106**, 7955–7966, 2000.
- De Haan, J., P. B. Bosma, and J. W. Hovenier, The adding method for multiple scattering of polarized light, *Astron. Astrophys.*, **183**, 371–391, 1986.
- Francis, P. N., A. Jones, R. W. Saunders, K. P. Shine, A. Slingo, and Z. Sun, An observational and theoretical study of the radiative properties of cirrus: Some results from ICE'89, *Q. J. R. Meteorol. Soc.*, **120**, 809–848, 1994.
- Giraud, V., J. C. Buriez, Y. Fouquart, and F. Parol, Large scale analysis of cirrus clouds from AVHRR data: Assessment of both a microphysical index and the cloud top temperature, *J. Appl. Meteorol.*, **36**, 664–675, 1997.
- Heymsfield, A. J., Cirrus uncinus generating cells and the evolution of cirriform clouds, I, Aircraft observations of the growth of the ice phase, *J. Atmos. Sci.*, **32**, 799–807, 1975.
- Heymsfield, A. J., Microphysical structure of stratiform and cirrus clouds, in *Aerosol-Cloud-Climate Interactions*, *Int. Geophys. Ser.*, vol. 54, edited by P. V. Hobbs, 233 pp., Academic, San Diego, Calif., 1993.
- Heymsfield, A. J., and C. M. R. Platt, A parameterization of the particle size spectrum of ice clouds in terms of the ambient temperature and the ice water content, *J. Atmos. Sci.*, **41**, 846–855, 1984.
- Inoue, T., On the temperature and the effective emissivity determination of semi-transparent clouds by bi-spectral measurements in the  $10\ \mu\text{m}$  window region, *J. Meteorol. Soc. Jpn.*, **63**, 88–98, 1985.
- Krupp, C., Holographic measurements of ice crystals in cirrus clouds during the International Cloud Experiment ICE 89: Report of the 4th ICE/EUCREX Workshop, report, Laboratoire d'Optique Atmosphérique, Univ. des Sci. et Tech. de Lille, Lille, France, 1991.
- Liao, X., W. B. Rossow, and D. Rind, Comparison between SAGE II and ISCCP high level clouds, I, Global and zonal mean cloud amounts, *J. Geophys. Res.*, **100**, 1121–1135, 1995.
- Liou, K. N., Influence of cirrus clouds on weather and climate processes: A global perspective, *Mon. Weather Rev.*, **114**, 1167–1199, 1986.
- Mace, G. G., T. P. Ackerman, P. Minnis, and D. F. Young, Cirrus layer microphysical properties derived from surface-based millimeter radar and infrared interferometer data, *J. Geophys. Res.*, **103**, 23,207–23,216, 1998.
- Macke, A., J. Mueller, and E. Raschke, Single scattering properties of atmospheric ice crystal, *J. Atmos. Sci.*, **53**, 2813–2825, 1996a.
- Macke, A., M. I. Mishchenko, and B. Cairns, The influence of inclusions on light scattering by large ice particles, *J. Geophys. Res.*, **101**, 23,311–23,316, 1996b.
- McFarquhar, G. M., and A. J. Heymsfield, Microphysical characteristics of three cirrus anvils sampled during the Central Equatorial Pacific Experiment (CEPEX), *J. Atmos. Sci.*, **52**, 2401–2423, 1996.
- Minnis, P., P. W. Heck, and D. F. Young, Inference of cirrus cloud properties from satellite observed visible an infrared radiances, II, Verification of theoretical radiative properties, *J. Atmos. Sci.*, **50**, 1305–1322, 1993.
- Minnis, P., D. F. Young, B. A. Baum, P. W. Heck, and S. Mayor, A near-global analysis of cloud microphysical properties using multispectral AVHRR data, paper presented at 9th Conference on Atmospheric Radiation, Am. Meteorol. Soc., Long Beach, Calif., 2–7 February 1997.
- Minnis, P., D. P. Garber, D. F. Young, R. F. Arduini, and Y. Takano, Parameterizations of reflectance and effective emittance for satellite remote sensing of cloud properties, *J. Atmos. Sci.*, **55**, 3313–3339, 1998.
- Minnis, P., D. F. Young, B. A. Wielicki, P. W. Heck, S. Sun-Mack, and T. D. Murray, Cloud properties derived from VIRS for CERES, paper presented at 10th Conference on Atmospheric Radiation, Am. Meteorol. Soc., Madison, Wis., 28 June to 2 July 1999.
- Mishchenko, M. I., L. D. Travis, and A. Macke, Light scattering by non-spherical particles in the atmosphere: An overview, paper presented at International Radiation Symposium 96: Current Problems in Atmospheric Radiation, Am. Geophys. Union, Fairbanks, Alaska, 19–24 August 1996.
- Nguyen, L., P. Minnis, J. K. Ayers, W. L. Smith Jr., and S. P. Ho, Inter-calibration of geostationary and polar satellite data using AVHRR, VIRS,

- and ATSR-2 data, paper presented at 10th Conference on Atmospheric Radiation, Am. Meteorol. Soc., Madison, Wis., 28 June to 2 July 1999.
- Randall, D., B. Albrecht, S. Cox, D. Johnson, P. Minnis, W. Rossow, and D. Starr, On FIRE at ten, *Adv. Geophys.*, *38*, 37–177, 1996.
- Raschke, E., P. Flamant, Y. Fouquart, P. Hignett, H. Isaka, P. R. Jonas, H. Sundquist, and P. Wendling, Cloud radiation studies during the European Cloud Radiation Experiment (EUCREX), *Surv. Geophys.*, *19*, 89–138, 1998.
- Rossow, W. B., and R. A. Schiffer, Advances in understanding clouds from ISCCP, *Bull. Am. Meteorol. Soc.*, *80*, 2261–2287, 1999.
- Spinhirne, J. D., W. D. Hart, and D. L. Hlavka, Cirrus infrared parameters and shortwave reflectance relations from observations, *J. Atmos. Sci.*, *53*, 1438–1458, 1996.
- Takano, Y., and K. N. Liou, Solar radiative transfer in cirrus clouds, I, Single-scattering and optical properties of hexagonal ice crystals, *J. Atmos. Sci.*, *46*, 3–19, 1989.
- Takano, Y., and K. N. Liou, Radiative transfer in cirrus clouds, III, Light scattering by irregular ice crystal, *J. Atmos. Sci.*, *52*, 818–837, 1995.
- Toon, O. B., and R. C. Mialke-Lye, Subsonic Aircraft: Contrail and Cloud Effects Special Study (SUCCESS), *Geophys. Res. Lett.*, *25*, 1109–1112, 1998.
- Valero, F. P. J., J. Herman, P. Minnis, W. D. Collins, R. Sadourny, W. Wiscombe, D. Lubin, and K. Ogilvie, Triana-a Deep Space Earth and Solar Observatory, background report, NASA, Greenbelt, Md., 1999. (Available at <http://Triana.gsfc.nasa.gov/home>)
- Wendling, P., R. Wendling, and H. K. Weickmann, Scattering of solar radiation by hexagonal ice crystals, *Appl. Opt.*, *18*, 2663–2671, 1979.
- Yang, P., and K. N. Liou, Finite difference time-domain method for light scattering by small ice crystals in three dimensional space, *J. Opt. Soc. Am. A Opt. Image Sci.*, *13*, 2072–2085, 1996.
- Yang, P., and K. N. Liou, Single scattering properties of complex ice crystals in terrestrial atmosphere, *Contrib. Atmos. Phys.*, *71*, 223–248, 1998.
- Yang, P., K. N. Liou, K. Wyser, and D. Mitchell, Parameterization of the scattering and absorption properties of individual ice crystals, *J. Geophys. Res.*, *105*, 4699–4718, 2000.
- Yang, P., B.-C. Gao, B. A. Baum, W. J. Wiscombe, Y. X. Hu, S. L. Nasiri, P. F. Soulen, A. J. Heymsfield, G. M. McFarquhar, and L. M. Miloshevich, Sensitivity of cirrus bidirectional reflectance to vertical inhomogeneity of ice crystal habits and size distributions for two Moderate-Resolution Imaging Spectroradiometer (MODIS) bands, *J. Geophys. Res.*, *106*, 17,267–17,292, 2001.
- 
- R. F. Arduini, P. Minnis, L. Nguyen, and D. Young, NASA/Langley Research Center, Mail Stop 420, Hampton, VA 23681-0001, USA. (r.f. arduini@larc.nasa.gov; p.minnis@larc.nasa.gov; l.nguyen@larc.nasa.gov; d.young@larc.nasa.gov)
- H. Chepfer, Laboratoire de Meteorologie Dynamique, Ecole Polytechnique, 91128 Palaiseau, France. (chepfer@lmd.polytechnique.fr)